Granular column collapse on slope: Effect of permeability on the runout characteristics

Krishna Kumar, Jean-Yves Delenne, Kenichi Soga

Abstract: This paper investigates the effect of permeability on the runout characteristics of collapse of granular columns on slopes in fluid. Two-dimensional sub-grain scale numerical simulations are performed to understand the flow dynamics of granular collapse in fluid. The Discrete Element (DEM) technique is coupled with the Lattice Boltzmann Method (LBM), for fluid-grain interactions, to understand the evolution of submerged granular flows. The fluid phase is simulated using Multiple-Relaxation-Time LBM (LBM-MRT) for numerical stability. In order to simulate interconnected pore space in 2D, a reduction in the radius of the grains (hydrodynamic radius) is assumed during LBM computations. The collapse of granular column in fluid is compared with the dry cases to understand the effect of fluid on the runout behaviour. A parametric analysis is performed to assess the influence of the granular characteristics (initial packing) on the evolution of flow and run-out distances for slope angles of 5Â°. In order to understand the effect of permeability on granular flow down a slope angle of 5Â°, the collapse of a granular column with an initial aspect ratio of 0.8 is simulated with different permeabilities. The hydrodynamic radius of a loosely packed granular column is varied from r = 0.7 R (high permeability), 0.75 R, 0.8 R, 0.85 R to 0.9 R (low permeability). The granular flow dynamics is investigated by analysing the effect of hydroplaning, water entrainment and viscous drag on the granular mass. The mechanism of energy dissipation, shape of the flow front, water entrainment and evolution of packing density is used to explain the difference in the flow characteristics of granular column collapse in fluid.

1 Introduction

Catastrophic earth movement events, such as landslides, debris flows, rock avalanches and reservoir embankment failures, exemplify the potential consequences of an earth gravitational instability. Slope failure is a problem of high practical importance for both civil engineering structures and natural hazard management. The study described in this paper examines the stability of underwater slopes, which are caused by excess seepage or earthquakes. They can damage offshore structures nearby and may generate a tsunami.

In order to describe the mechanism of underwater granular flows, it is necessary to consider both the dynamics of the solid phase of granular matter and the role of the ambient fluid, which exists

either inside the pores of the granular body and as free water outside the granular body (Denlinger and R. Iverson, 2001; R. M. Iverson, 1997). Initial acceleration plays a crucial role in underwater landslide propagation (Romano et al., 2017), as the initial acceleration increases, there is a limited time for the landslide to deform during the acceleration phase. The initiation and propagation of submarine granular flows depend mainly on geometry (e.g. slope angle, lateral extent, etc), initial stress conditions, density, soil properties, and the quantity of the material destabilised. Although certain macroscopic models are capable of capturing simple mechanical behaviour (e.g. Topin et al. (2011)), the complex fundamental mechanism that occurs at the grain scale, such as hydrodynamic instabilities, the formation of clusters, collapse, and transport, require further investigation in order to make better engineering assessment of the potential risk of damages against underwater slope failures for example.

The momentum transfer between the discrete and the continuous phases of fluid saturated granular material significantly affects the dynamics of the flow (Peker and Helvaci, 2007). The grain-scale description of the granular material enriches the macro-scale variables. In particular, when the solid phase reaches a high-volume fraction, it is important to consider the strong heterogeneity arising from the contact forces between the grains, the drag interactions which counteract the movement of the grains, and the hydrodynamic forces that reduce the weight of the grains inducing a transition from a dense compacted to a dense suspended flow (Meruane et al., 2010).

The case of granular material movements in presence of an interstitial fluid at the grain-scale has been less studied. In this paper, we report the findings of the study on the granular column collapse in fluid in the inclined configuration using the coupled Lattice Boltzmann Method (LBM) and Discrete Element Method (DEM). We examined the effect of density and slope angle on the runout evolution.

The Lattice Boltzmann Method is a 'micro-particle' based numerical time-stepping procedure for the solution of incompressible fluid flows. Consider a 2D incompressible fluid flow with density ρ and kinematic viscosity v, in a rectangular domain $\boldsymbol{D}$. The fluid domain is divided into a rectangular grid or lattice, with the same spacing *'h'* in both the x- and the y-directions, as shown in fig. 1. The present study focuses on two-dimensional problems, hence the *D2Q9* momentum discretisation is adopted (see (He et al., 1997) for naming convention).

The lattice Boltzmann Bhatnagar-Gross-Krook (LGBK) method is capable of simulating various hydrodynamics (Succi, 2001) and offers intrinsic parallelism. Although LBM is successful in modelling complex fluid systems, such as multiphase flows and suspensions in fluid, the LBM may lead to numerical instability when the dimensionless relaxation time τ is close to 0.5. The Multi-Relaxation Time Lattice Boltzmann Method (LBM-MRT) overcomes the deficiencies of linearlised single relaxation LBM-BGK, such as fixed Prandtl number (Pr=ν/κ), where the thermal conductivity 'κ' is unity (Liu et al., 2003). The LB-MRT model offers better numerical stability and has more degrees of freedom. In the formulation of the linear Boltzmann equation with multiple relaxation time approximation, the lattice Boltzmann equation is written as:

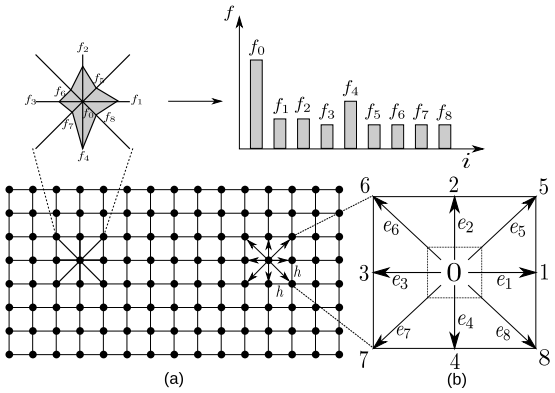

Figure 1: The Lattice Boltzmann discretisation and D2Q9 scheme: (a) a standard LB lattice and histogram views of the discrete single particle distribution function/direction-specific densities f_i; (b) D2Q9 model

$$f_\alpha(\mathbf{x} + \mathbf{e}_i\Delta_t, t + \Delta_t) - f_\alpha(\mathbf{x},t) = -\mathbf{S}_{\alpha i}(f_i(\mathbf{x},t) - f_i^{eq}(\mathbf{x},t) \quad (1)$$

where $\mathbf{S}$ is collision matrix. The nine eigen values of $\mathbf{S}$ are all between 0 and 2 so as to maintain linear stability and the separation of scales, which means that the relaxation times of non-conserved quantities are much faster than the hydrodynamic time scales. The LGBK model is the special case in which the nine relaxation times are all equal and the collision matrix $\mathbf{S} = \frac{1}{\tau}\mathbf{I}$, where $\mathbf{I}$ is the identity matrix. The evolutionary progress involves two steps, advection and flux. The advection can be mapped to the momentum space by multiplying through by a transformation matrix $\mathbf{M}$ and the flux is still finished in the velocity space. The evolutionary equation of the multi-relaxation time lattice Boltzmann equation is written as:

$$\mathbf{f}(\mathbf{x} + \mathbf{e}_i\Delta_t, t + \Delta_t) - \mathbf{f}(\mathbf{x},t) = -M^{-1}\hat{\mathbf{S}}(\hat{\mathbf{f}}(\mathbf{x},t) - \hat{\mathbf{f}}^{eq}(\mathbf{x},t)) \quad (2)$$

where $\mathbf{M}$ is the transformation matrix mapping a vector $\mathbf{f}$ in the discrete velocity space $\mathbb{V} = \mathbb{R}^b$ to a vector $\hat{\mathbf{f}}$ in the moment space $\mathbb{V} = \mathbb{R}^b$.

$$\hat{\mathbf{f}} = \mathbf{M}\mathbf{f} \quad (3)$$

$$\mathbf{f}(\mathbf{x},t) = [f_0(\mathbf{x},t), f_1(\mathbf{x},t), \ldots f_8(\mathbf{x},t)]^T \quad (4)$$

The collision matrix $\hat{\mathbf{S}} = MSM^{-1}$ in moment space is a diagonal matrix: $\hat{\mathbf{S}} = \text{diag}\,[s_1, s_2, s_3, \ldots s_9]$. The transformation matrix $\mathbf{M}$ can be constructed via Gram-Schmidt orthgonalisation procedure.

Through the Chapman-Enskog expansion (Du et al., 2006), the incompressible Navier-Stokes equation can be recovered and the viscosity is given as:

$$\nu = c_s^2 \Delta t(\tau - 0.5) \tag{5}$$

1.1 Turbulence in Lattice Boltzmann Method

Modelling fluids with low viscosity like water remains a challenge, necessitating very small values of *h*, and/or τ very close to 0.5 (He et al., 1997). Turbulent flows are characterised by the occurrence of eddies with multiple scales in space, time and energy. In this study, the Large Eddy Simulation (LES) is adopted to solve for turbulent flow problems. The separation of scales is achieved by filtering of the Navier-Stokes equations, from which the resolved scales are directly obtained and unresolved scales are modelled by a one-parameter Smagorinski sub-grid methodology, which assumes that the Reynold's stress tensor is dependent only on the local strain rate (Smagorinsky, 1963). The turbulent viscosity ν is related to the strain rate S_{ij} and a filtered length scale 'h' as follows:

$$v_t = (S_c h)^2 \overline{S}; \tag{6}$$

$$\overline{S} = \sqrt{\sum_{i,j} \tilde{S}_{i,j} \tilde{S}_{i,j}} \tag{7}$$

where S_c is the Smagorinski constant found to be close to 0.03 (Yu et al., 2005).

The effect of the unresolved scale motion is taken into account by introducing an effective collision relaxation time scale τ_t, so that the total relaxation time τ_* is written as:

$$\tau_* = \tau + \tau_t \tag{8}$$

where τ and τ_t are respectively the standard relaxation times corresponding to the true fluid viscosity *v* and the turbulence viscosity v_t, defined by a sub-grid turbulence model. The new viscosity v_* corresponding to τ_* is defined as:

$$v_* = v + v_t = \frac{1}{3}(\tau + \tau_t - \frac{1}{2}) C^2 \Delta t \tag{9}$$

$$v_t = \frac{1}{3} \tau_t C^2 \Delta t \tag{10}$$

The Smagorinski model is easy to implement and the Lattice Boltzmann formulation remains unchanged, except for the use of a new turbulence-related viscosity τ_*. The component s_1 of the collision matrix becomes $s_1 = \frac{1}{\tau + \tau_t}$.

2 Coupled LB-DEM model

2.1 General

The Lattice Boltzmann approach has the advantage of accommodating large particle sizes and the interaction between the fluid and the moving particles can be modelled through relatively simple fluid - particle interface treatments. Further, employing the Discrete Element Method (DEM) to account for the particle/particle interaction naturally leads to a combined LB - DEM solution procedure. The Eulerian nature of the Lattice Boltzmann formulation, together with the common explicit time step scheme of both the Lattice Boltzmann and the Discrete Element, makes this coupling strategy an efficient numerical procedure for the simulation of particle-fluid systems (Cook et al., 2004). The LB-DEM coupling system is a powerful fundamental research tool for investigating hydro-mechanical physics in porous media flow. To capture the actual physical behaviour of a fluid-particle system, the boundary condition between the fluid and the particle is modelled as a non-slip boundary condition, i.e. the fluid near the particle should have a similar velocity as the particle boundary. The solid particles inside the fluid are represented as solid lattice nodes. The discrete nature of lattice will result in stepwise representation of the surfaces (Kumar, 2015). A very small lattice spacing is adopted to obtain smoother boundaries.

The smallest DEM grain in the system controls the size of the lattice. In the present study, a very fine resolution of $d_{min}/h = 10$ is adopted. That is, the smallest grain with a diameter dmin in the system is discretized into 100 lattice nodes ($10h \times 10h$). This provides a very accurate representation of the interaction between the solid and the fluid nodes.

When combining the Discrete Element modelling of grain interactions with the lattice Boltzmann formulation, an issue arises. That is, there are now two time steps: Δt for the fluid flow and Δt_D for the particle movements. Since Δt_D is normally smaller than Δt, Δt_D is slightly reduced to a new value Δt_s so that Δt and Δt_s have an integer ratio n_s:

$$\Delta t_s = \Delta t / n_s \tag{11}$$

$$n_s = [\Delta t / \Delta t_D] + 1 \tag{12}$$

This results in a subcycling time integration for the Discrete Element part. Δt every step of the fluid computation, n_s sub-steps of integration are performed for DEM using the time step Δt_s. The hydrodynamic force is unchanged during this sub-cycling.

2.2 Modelling Permeability

In DEM, the grain – grain interaction is described based on the contact interactions. In a 3D granular assembly, the pore spaces between grains are interconnected, whereas in 2-D assembly,

the grains are in contact with each other that result in a non-interconnected pore-fluid space. This results in a no flow condition in a 2-D case (see fig. 2). In order to overcome this difficulty, a reduction in radius is assumed only during LBM computations (fluid and fluid–solid interaction), which is called the hydrodynamic radius. The hydrodynamic radius allows interconnected pore space through which the surrounding fluid can flow (hydrodynamic radius r = 0.7 R to 0.95 R, where 'R' is the grain radius). The hydrodynamic radius is used only during the LBM computations, and has no effect on the grain–grain interactions computed using DEM. Different values of macroscopic permeability can be obtained for any given initial packing by varying the hydrodynamic radius of the grains, without having to change the actual granular packing. This introduces a new parameter into the system. In a physical sense, a hydrodynamic radius represents the three-dimensional permeability of a granular assembly simulated as a two-dimensional geometry.

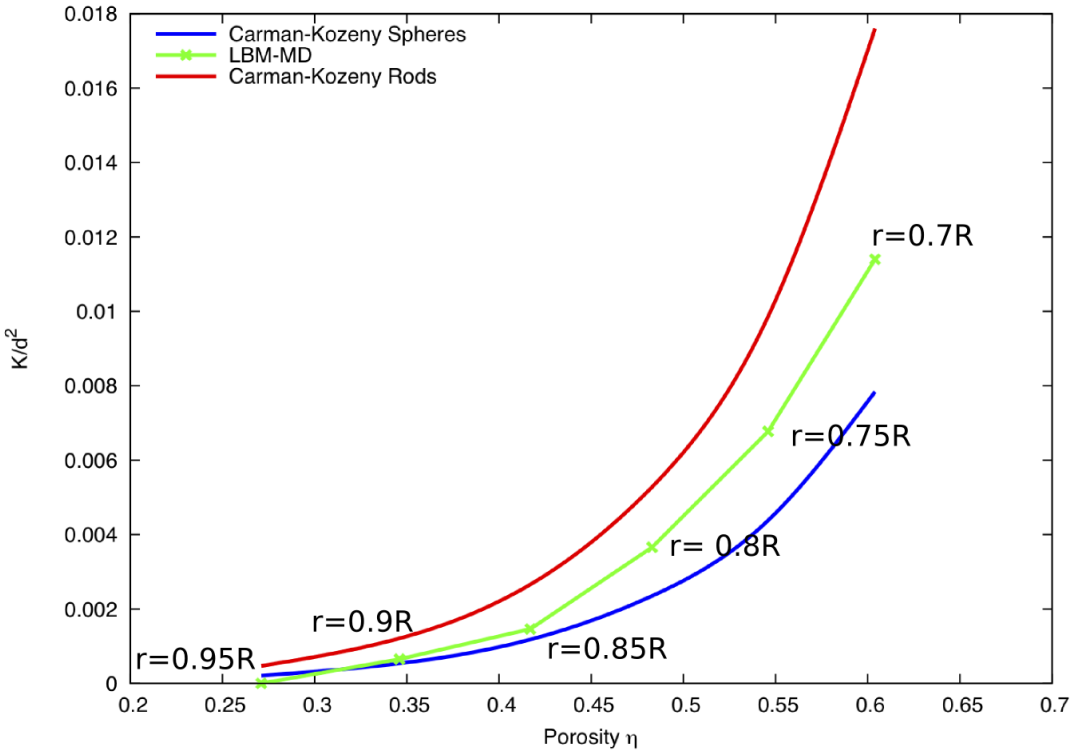

Figure 2: Relation between permeability and porosity for different hydrodynamic radius and comparison with the analytical solution.

In order to understand the relation between the hydrodynamic radius and the permeability of a granular assembly, permeability tests are performed by varying the hydrodynamic radius r as 0.7 R, 0.75 R, 0.8 R, 0.85 R, 0.9 R and 0.95 R. The permeability values obtained are normalized by the square of the average grain diameter following the Carman-Kozeny equations (Yazdchi et al., 2011). The comparison of normalised permeability from the 2D LB-DEM simulations with the Carman-Kozeny equations for spherical and cylindrical grain assembly for different porosities are presented in fig. 3. It can be observed from the figure that the permeability decreases drastically as the radius is decreased from 0.7R to 0.95R. The granular assembly is almost impermeable for a hydrodynamic radius of 0.95R. The normalized permeability is found to match the qualitative

trend of the Carman-Kozeny equations.

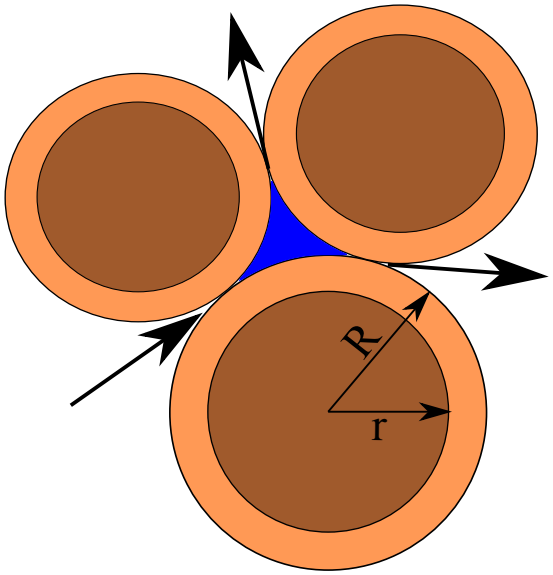

Figure 3: Schematic representation of the hydrodynamic radius in LBM-DEM computation.

3 Granular column collapse on slopes in fluid

3.1 Problem definition

In this study, a 2D polydisperse system ($d_{max}/d_{min} = 1.8$) of circular discs in fluid was used to understand the behaviour of granular flows on inclined planes. As shown in fig. 4, an inclined gravity direction was varied to examine the slope angle effect. The soil column was modelled using 1000 discs of density $2650\,\mathrm{kg/m^3}$ and a contact friction angle of $26°$. The aspect ratio 'a' is defined as the ratio of the initial height (H_i) to the width (L_i) of the column. A granular column of aspect ratio 'a' of 0.8 was used. The collapse of the column was simulated inside a fluid with a density of $1000\,\mathrm{kg/m^3}$ and a kinematic viscosity of $1 \times 10^{-6}\,\mathrm{m^2/s}$. The choice of a 2D geometry has the advantage of cheaper computational effort than a 3D case, making it feasible to simulate very large systems. To model 3D permeability nature of spheres as 2D discs, a reduction in radius: a hydrodynamic radius r = 0.9R was adopted only for LBM computations, as described earlier. Dry column collapse was also performed to study the effect of hydrodynamic forces on the runout distance. The runout distance is normalised with respect to the initial width of the column. The granular column collapse was allowed to flow down a slopes of $5°$.

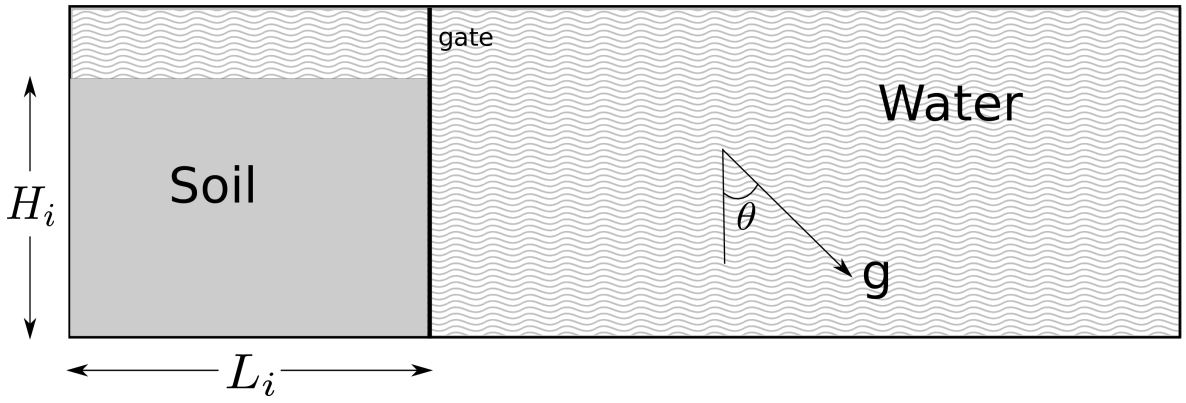

Figure 4: Underwater granular collapse set-up

4 Collapse of a dense granular column

Figure 5 shows the snapshots of the flow evolution of a dense granular column (aspect ratio 0.8), which has an initial packing density of $\Phi = 83\%$, on a $5°$ slope. The failure begins at the toe end of the column, and the shear-failure surface propagates into the column at an angle of about 45 - $50°$ The failure is due to collapse of the flank. Force chains can be observed in the static region of the column. Once the material is destabilised, the surface of the flowing granular mass interacts with the surrounding fluid, resulting in the formation of turbulent vortices. The vortices are formed only during the horizontal acceleration phase and interact with the grains at the surface resulting in an irregular free surface. As the granular material ceases to flow, force chains restart to develop at the flow front, revealing consolidation of the granular mass with an increase in the shear resistance. The vortices formed during the collapse start to raise above the settled granular mass.

The runout distance is measured by tracking the farthest particle that is still in contact with the main granular mass. The normalized runout distance is measured as $\Delta L = (L_f - L_i)/L_i$, where L_f is the runout distance at a given time and L_i is the initial width of the column. The time is normalised as t/τ_c, where τ_c is defined as the critical time of the dry granular column collapse to be fully mobilised on a horizontal plane ($\tau_c = \sqrt{(H/g)}$) (Staron and Hinch, 2007).

5 Effect of initial density - Loose versus Dense

Topin et al. (2011) observed from CFD-DEM simulations of granular collapse on a horizontal plane in different viscous fluids that, for a given initial geometry, the run-out distance in the dry case is significantly higher than the submerged case, an observation similar to the experimental results of Cassar et al. (2005). For a given geometry, the initial volume fraction of the granular mass has a significant effect on the morphology of the granular deposits in fluid (Rondon et al., 2011; Pailha et al., 2008). In the dry case, inertia is responsible for the enhanced mobility at steeper slopes. In the submerged cases, however, the grain-inertial effects remain negligible

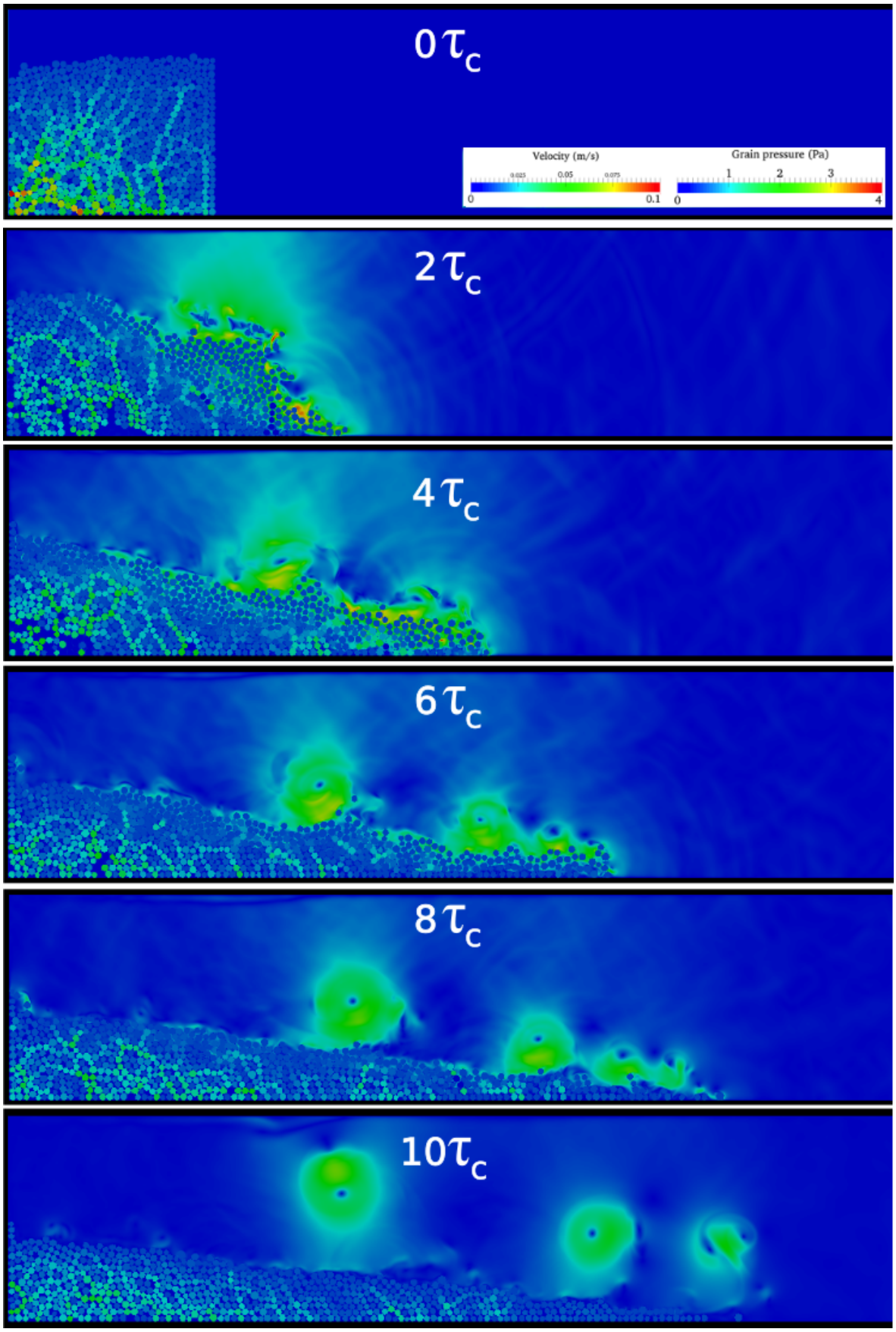

Figure 5: Evolution of a dense sand column (aspect ratio 0.8) on a slope of $5°$.

because of the predominance of viscous effects on the granular dynamics (Topin et al., 2011). This could explain the importance of the initial volume fraction on the runout behaviour of submerged granular columns. In this study, we examine the effect of initial packing density on the runout behaviour at 5° slope angle in both dry and submerged cases.

In order to understand the influence of the initial packing density on the runout behaviour, a collapse of loose sand column (initial packing density $\Phi = 79\%$) was simulated at 5° slope angle and the results are compared to the dense sand column cases (initial packing density $\Phi = 83\%$), which was presented earlier.

5.1 Effect of permeability

The effect of permeability on granular flow down a slope angle of 5° is investigated for the case of collapse of a granular column with an initial aspect ratio of 0.8 at different permeabilities. The hydrodynamic radius of a loosely packed granular column is varied from $r = 0.7\ R$ (high permeability), $0.75\ R$, $0.8\ R$, $0.85\ R$ to $0.9\ R$ (low permeability). The run-out distance is found to increase with decreasing permeability of the granular assembly (fig. 6a). The run-out distance for high permeability conditions ($r = 0.7\ R - 0.8\ R$) are lower than their dry counterparts. Although, a decrease in permeability resulted in an increase in the run-out distance, no significant change in the run-out behaviour is observed for a hydrodynamic radii of up to $0.8\ R$.

With a further decrease in permeability ($r = 0.85\ R$ and $0.9\ R$), the run-out distance in the fluid is longer than that observed in the dry condition. At a very low permeability ($r = 0.9\ R$), the flowing granular mass entrains more water at the base, which causes a reduction in the effective stress accompanied by a lubrication effect. This can be seen by a significant increase in the peak kinetic energy and the sustained duration of the peak energy, in comparison to the dry and the highly permeable conditions (fig. 7a). However, the permeability of the granular column did not have an influence on the evolution of height during the flow. But, the dry granular column tends to collapse more than the immersed granular column due to the lack of viscous dissipation (fig. 6b).

Positive pore-pressure generation at the base of the flow is observed for low permeability conditions. Inspection of the local packing density showed entrainment of water at the base of the flow, which can also be observed by the steep decrease in the packing density (fig. 7b) for the very low permeability condition ($r = 0.9\ R$). At the end of the flow ($t \geq 10 \times \tau_c$), the excess pore-pressure dissipates and the granular flows, irrespective of their permeability, reach almost the same packing density.

Figure 9 shows the effect of permeability on the run-out behaviour for a dense and a loose granular column collapse on a slope of 5° and 0°. In both cases, the run-out distance increases with increase in the hydrodynamic radius (decrease in permeability). However in the dense case, the run-out distance observed in the fluid is shorter than the dry condition. Whereas in the loose condition, the run-out distance increases significantly at low permeabilities and results in a longer run-out distance in the submerged condition in comparison to the dry granular collapse.

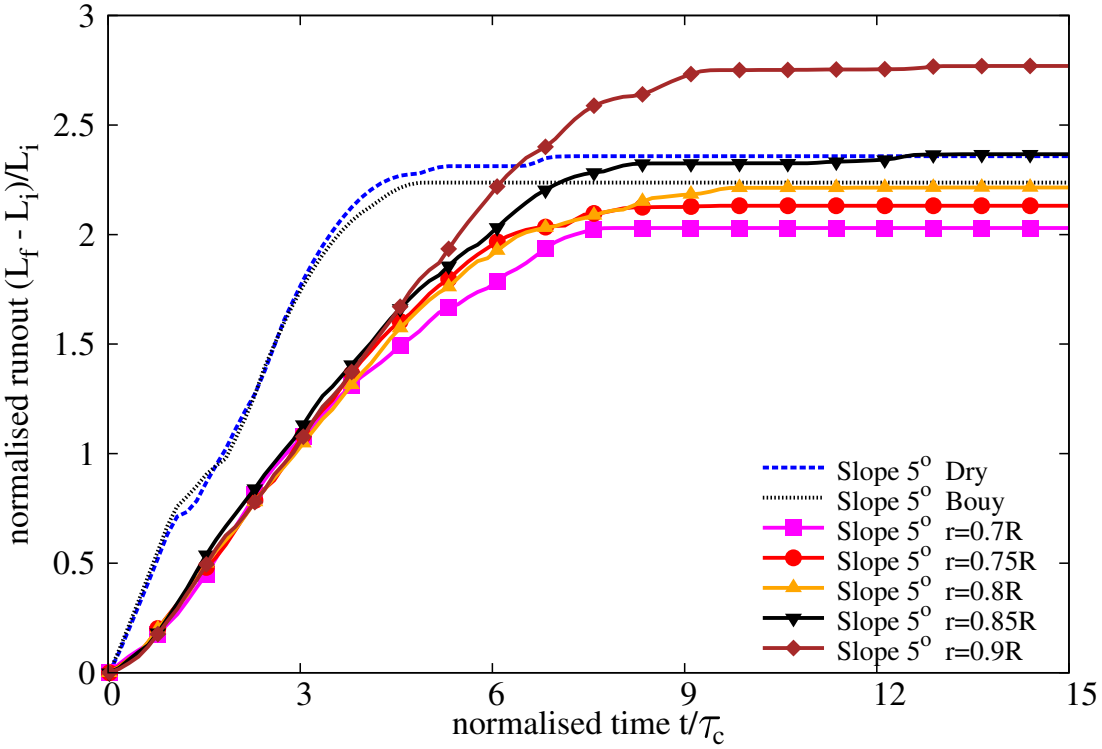

(a) Evolution of run-out with time.

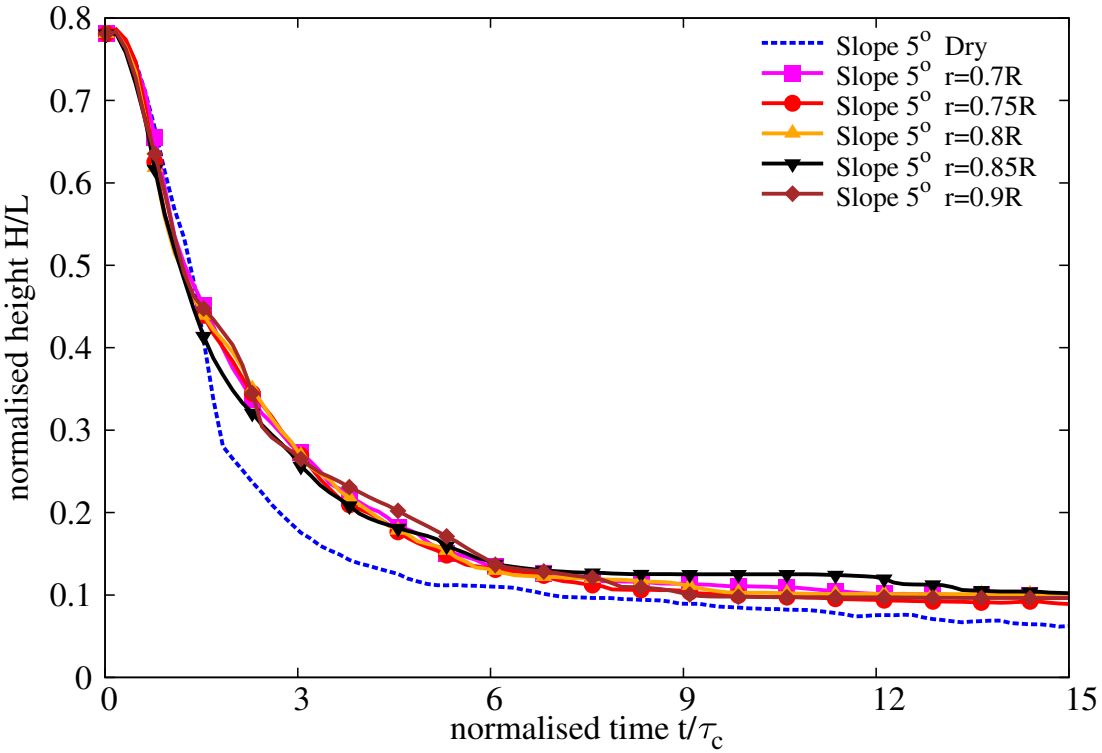

(b) Evolution of height with time.

Figure 6: Evolution of run-out and height with time for different permeability (loose slope 5°).

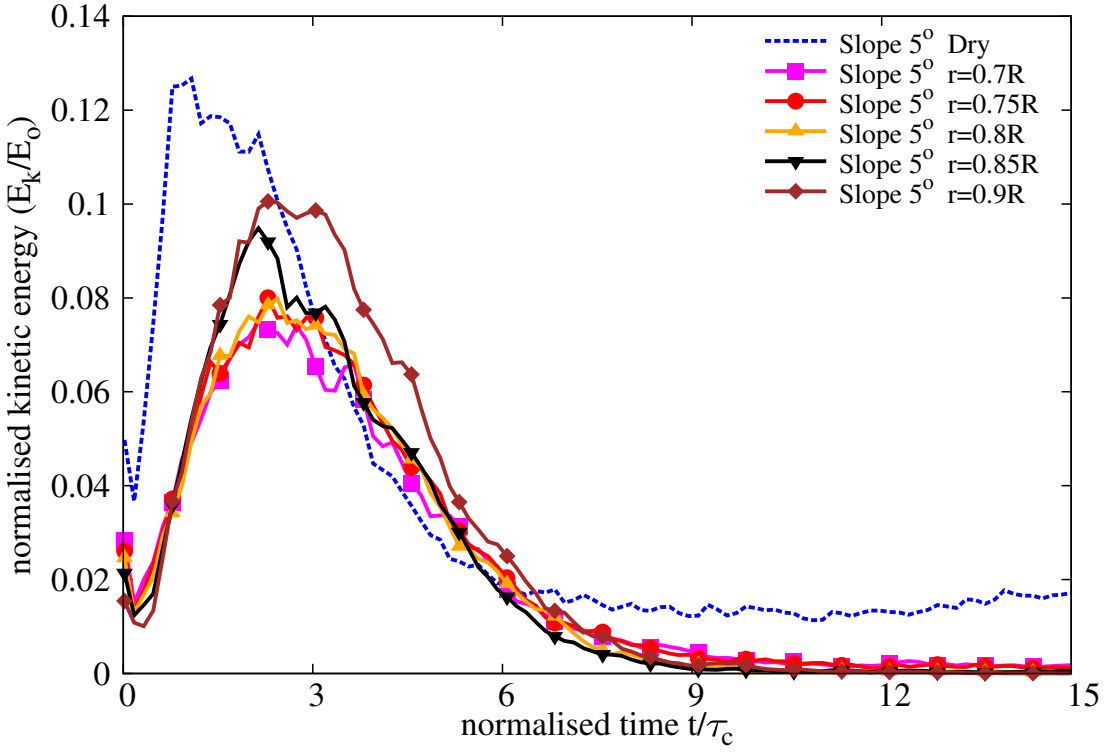

(a) Evolution of kinetic energy with time.

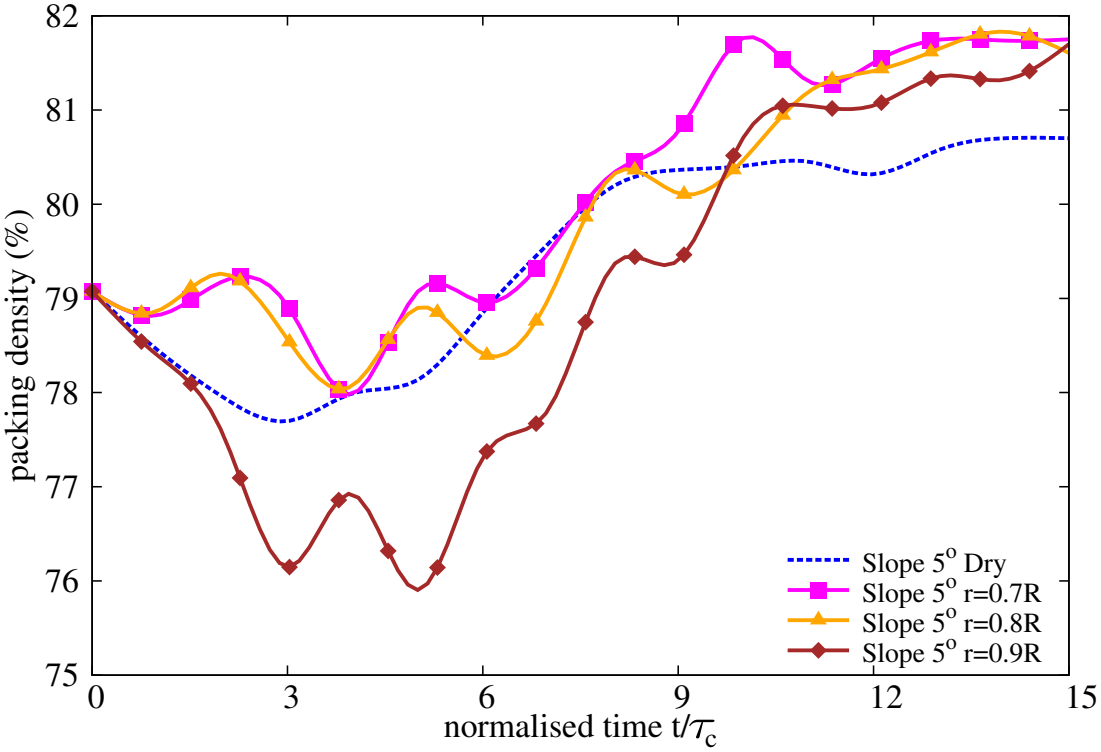

(b) Evolution of packing density with time.

Figure 7: Evolution of kinetic energy and packing density with time for different permeability (loose slope $5°$).

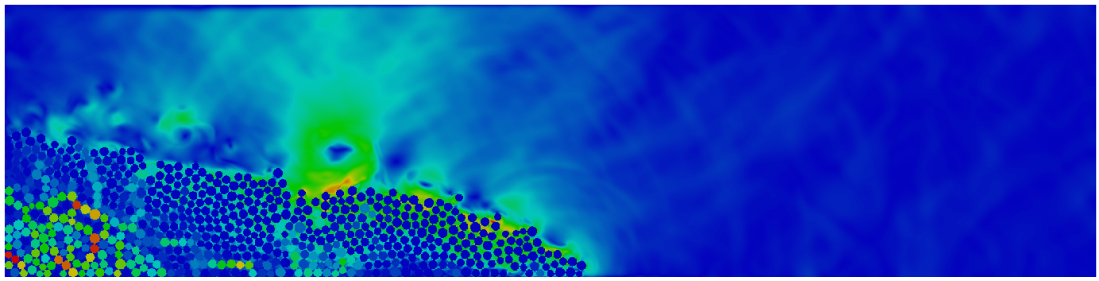

(a) r = 0.7 R

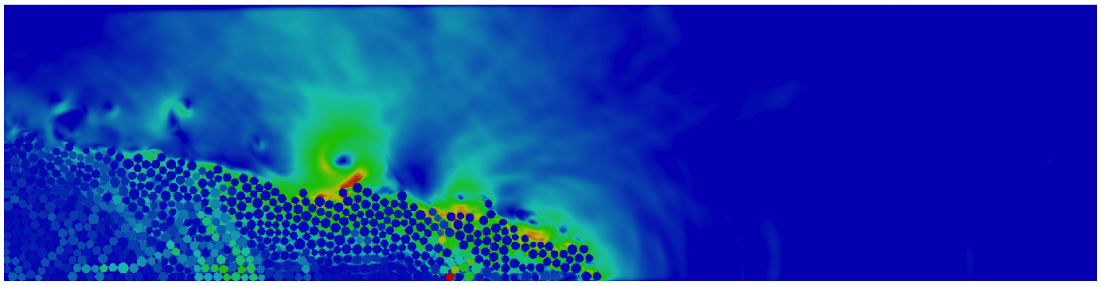

(b) r = 0.75 R

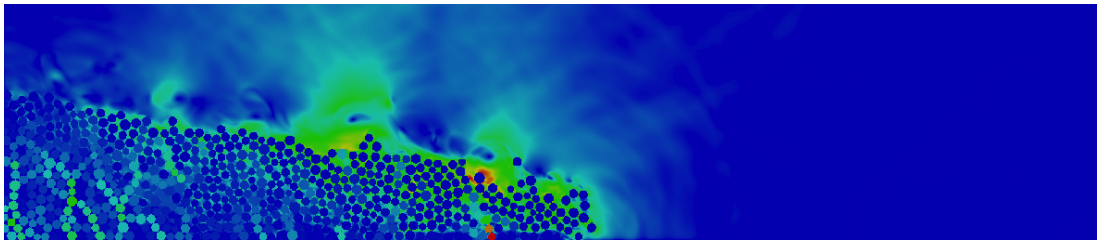

(c) r = 0.8 R

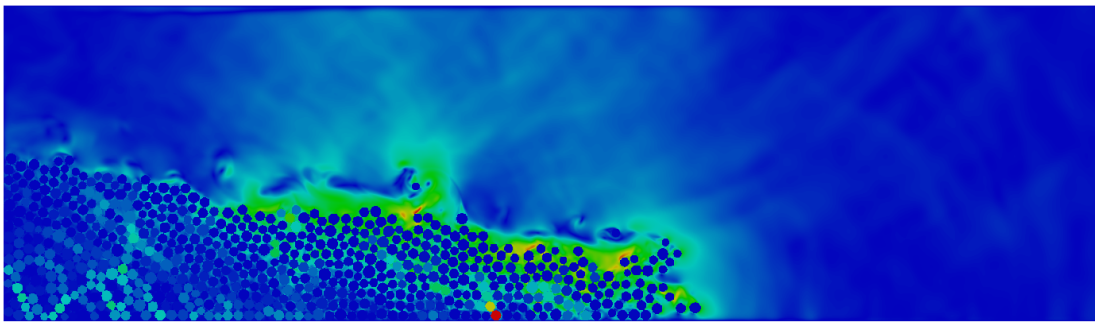

(d) r = 0.85 R

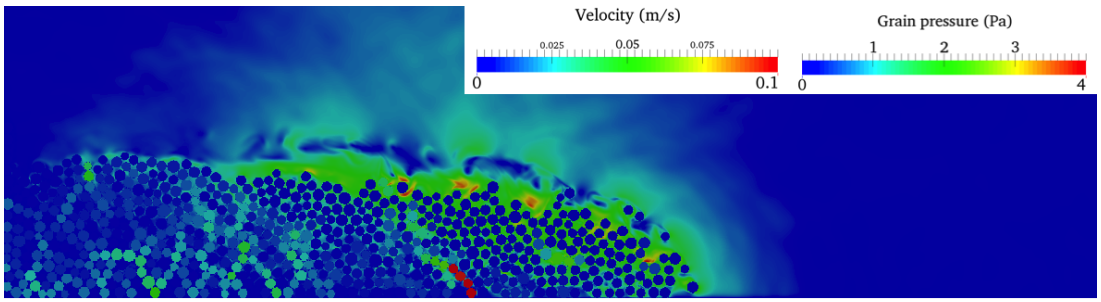

(e) r = 0.9 R

Figure 8: Evolution of the flow front at $t = 3\tau_c$ for different permeabilities (loose slope 5°).

The comparison of loose and dense collapse on slopes of 0° and 5° shows that the initial packing density plays a significant role in the case of collapse on a horizontal plane, however at a slope of 5°, the run-out distance is unaffected by the initial packing density at high permeability conditions. This shows that at high permeabilities, the viscous drag forces predominate resulting in almost the same run-out distance for both dense and loose conditions. However at a low permeability ($r = 0.9\ R$), hydroplaning is observed in the case of loose granular column resulting in a substantially longer run-out distance than the dense granular column in submerged condition.

6 Mechanisms of granular column collapse in fluid

The difference in the runout behaviour between the dense and loose granular columns suggests difference in runout mechanism. The collapse of a granular column involves three stages: an initiation stage characterised by a distinct failure surface, a runout phase characterised by horizontal acceleration which involves formation of eddies, and the final settlement phase. The mechanisms observed in each phase are discussed next.

6.1 Initiation phase

Comparing the initial evolution of runout between the loose and the dense cases ($t = 0$ to $3\tau_c$), see figs. 5 and 8, the loose granular columns evolve faster than their dense counterpart. When a granular material is sheared in the submerged conditions, it generates negative pore water pressure initially due to the undrained conditions. In the undrained conditions, the dilation movement (volume expansion) of the granular assembly by shearing self-generates negative excess pore pressure inside the pores. The fluid inside the pores does not have time to seep in or out from the free water outside the column by the internally generated pressure gradient between the pore space and the outside free water. The negative excess pore pressures produce larger interparticle forces by bringing the grains together. Macroscopically this results in increase in the mean effective stress and provides large shear resistance temporarily until the negative excess pore pressure dissipates with time. Large negative pore pressures were observed for the dense cases. Overcoming the region of large negative pore pressure translates to smaller kinetic energy and eventually a shorter runout distance for the dense granular columns.

The degree of dilation upon shearing is smaller in the loose granular column case than the dense case. Positive pore pressures can be observed along the failure plane. Positive pore pressures imply that the grains are pushing apart by increasing pore pressure during the initial phase of the collapse. The intergranular forces (or effective stress) are reduced and consequently the shear resistance decreases. This results in faster initiation and runout behaviour for the loose granular columns compared to the dense granular columns (Kumar et al., 2017).

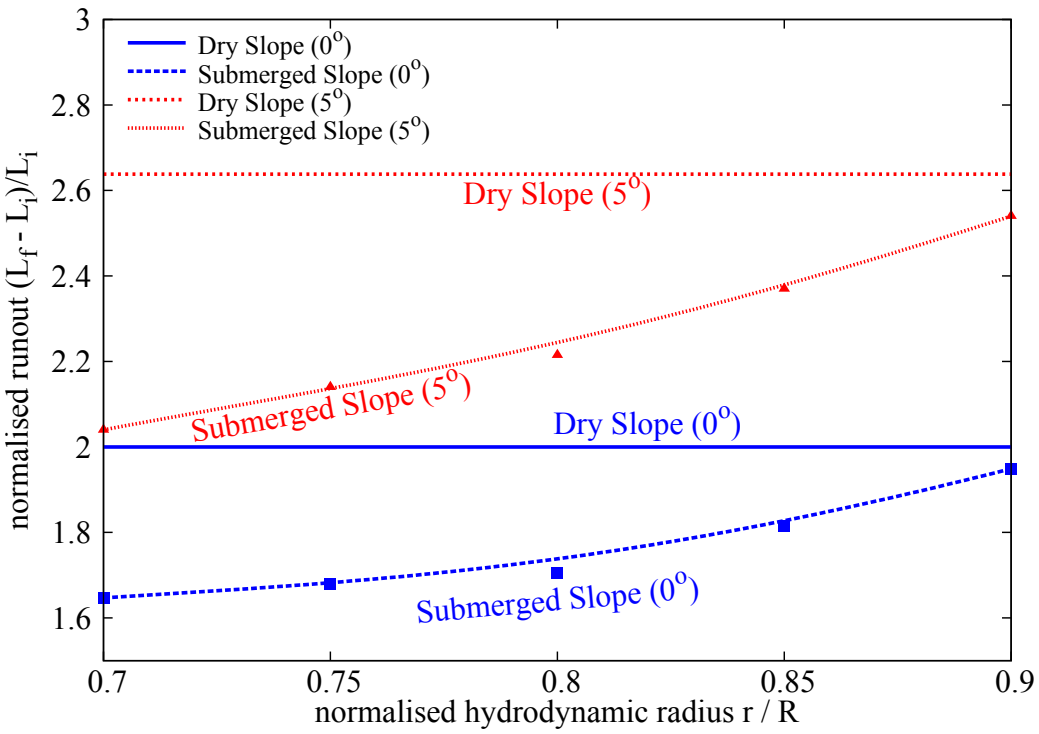

(a) Dense

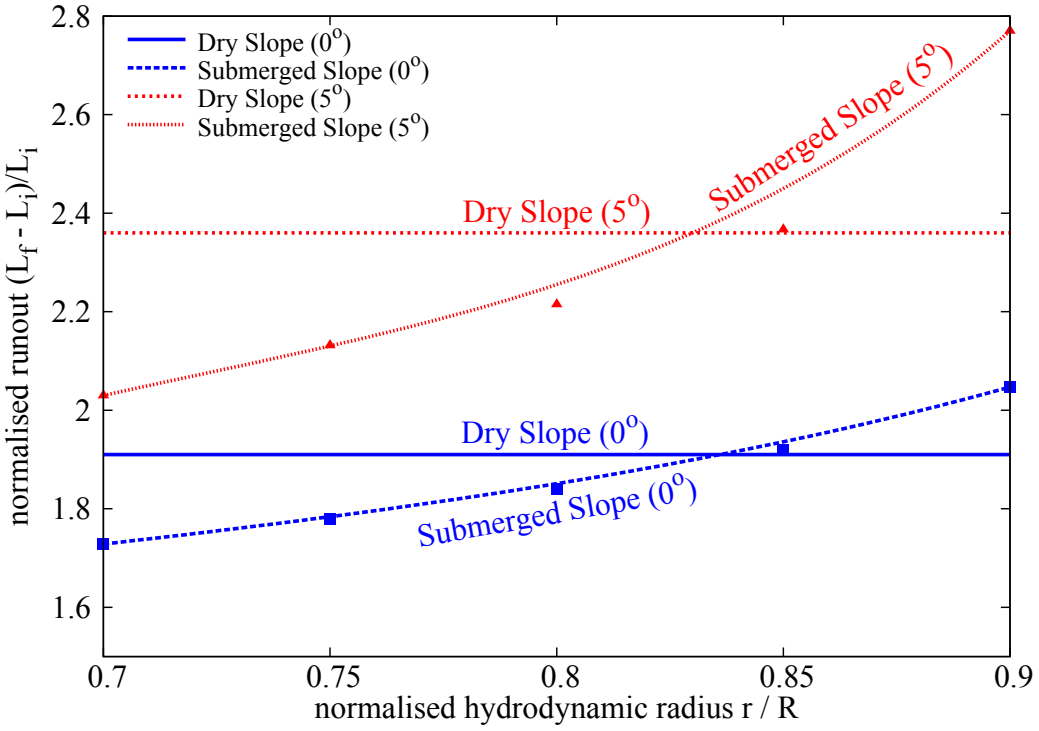

(b) Loose

Figure 9: Comparison between dry and submerged granular column for a slope angle of 0° and 5° on the effect of permeability on the run-out distance (Dense and Loose).

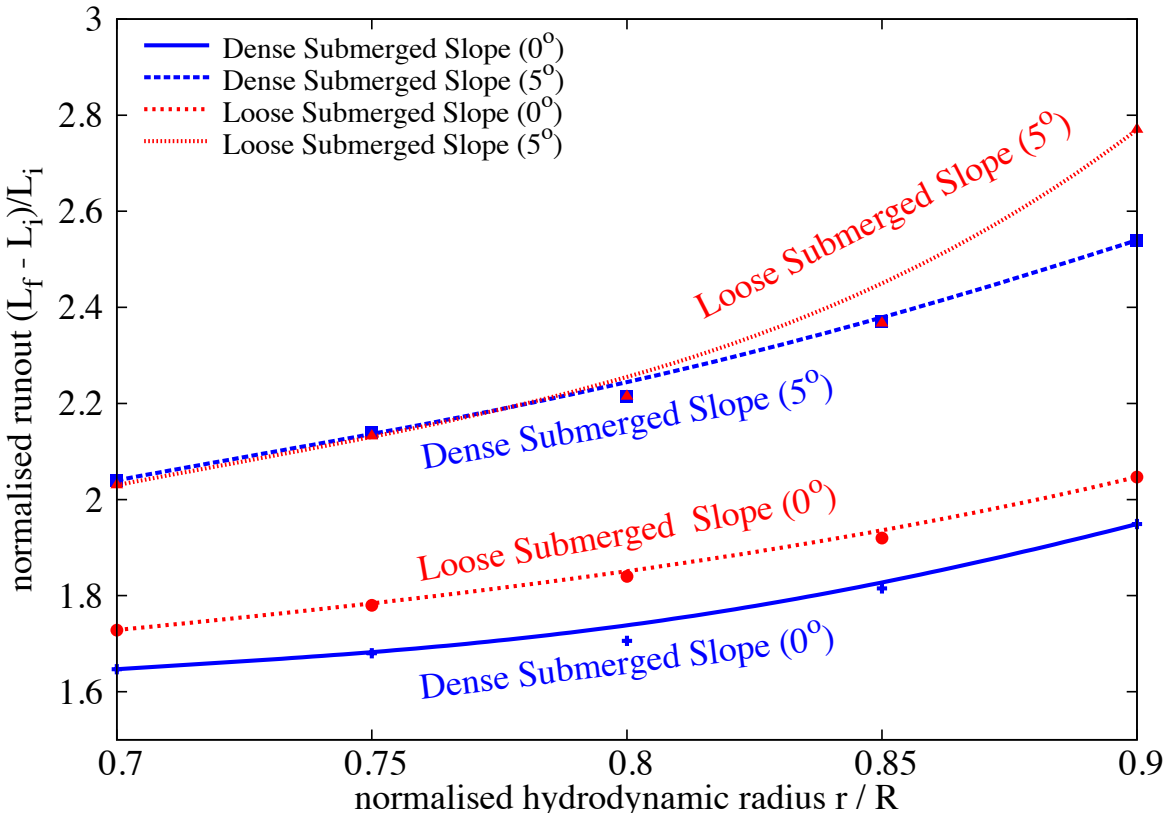

Figure 10: Effect of permeability on the run-out behaviour for different slope angle and the initial packing density.

6.2 Runout phase

In the second phase, the initial vertical collapse motion is converted to horizontal acceleration. The flow is fully mobilised at $3\tau_c$, when the kinetic energy is at its peak. In the submerged cases, the dynamics of the granular flow are controlled by the following three factors: (a) hydroplaning, defined as the loss of friction between the flowing material and the bottom surface due to the presence of water, (b) water entrainment at the front of the flowing mass, which results in a decrease in the density of the flowing granular mass, and (c) the interaction of the surface of granular flow with the surrounding fluid resulting in formation of eddies and drag effects. The role of water on the dynamics of the dense and loose granular columns is discussed in this section.

6.2.1 Hydroplaning

Hydroplaning refers to the loss of friction, which occurs due to the entrapment of water between the granular mass and the slope, which results in zero effective stresses. Figure 11 shows the effective stress of the flow front for a distance of $15d$ for the slope angle $5°$ case. The effective stress is computed from the contact forces acting between the grains and the bottom surface. The

horizontal axis is normalised to the maximum length of $15d$ from the flow front and the vertical axis is normalised to the initial maximum effective stress. The average effective stress at the bottom of the flowing granular mass over 5 time-steps is presented to avoid fluctuations in the stresses. The loose granular columns have zero average effective stress at the flow front ($7.5d$ from the front). In contrast, the dense granular columns that have positive effective stress at the sliding interface, which creates frictional forces that work against the flow movement. The loose granular flow tends to entrain more water at the base of the flow front, creating a hydroplaning surface. This results in a longer runout distance. This corroborates the influence of hydroplaning on the loose granular columns which show higher sustained peak kinetic energy in comparison with the dense granular columns.

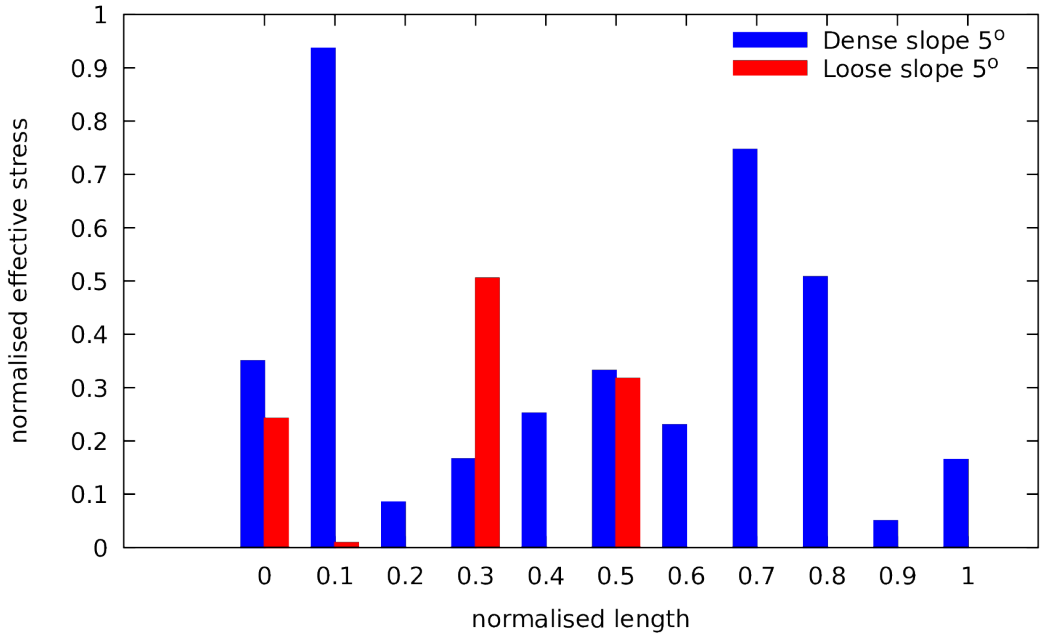

Figure 11: Effective stress at the flow front ($15d$) between the dense and loose submerged cases for a slope angle of $5°$ at time $t = 3\tau_c$

6.2.2 Water entrainment

Comparing the snapshots of the granular flow at time $t = 3\tau_c$ for the dense column cases fig. 5 and the loose column cases fig. 8, it can be seen that the overall shapes of the flow front are different. Figure 12 shows the boundary of the flowing mass and its evolution with time for the slope angle $5°$ case. It shows that the dense granular columns exhibit a more acute angle of attack (flow front) in contrast to a more parabolic profile for the loose granular columns. This difference in angle of flow front changes the ratio of amount of water entering the flowing granular mass to the water interacting with the surface of the granular mass. Figure 13 shows the horizontal velocity of the fluid and streamlines at the flow front of the dense and loose granular columns for the slope angle of $5°$. The density of streamlines entering the granular front is significantly higher for the loose column case, in comparison to the dense column case. This clearly shows

the effect of the shape of flow front on water entrainment. More water entrainment results in increase in pore space (or decrease in solid fraction) at the flow front, which in turn reduces the interparticle shear resistance.

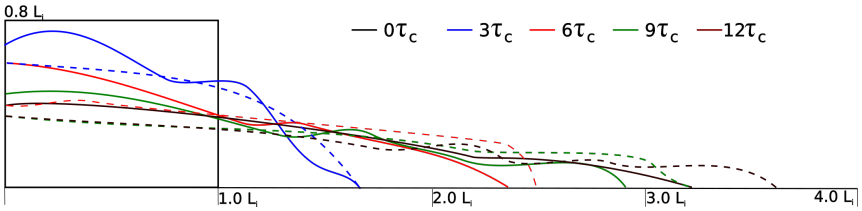

Figure 12: Profile outline evolution for dense (solid line) and loose (dashed line) cases for a slope of $5°$

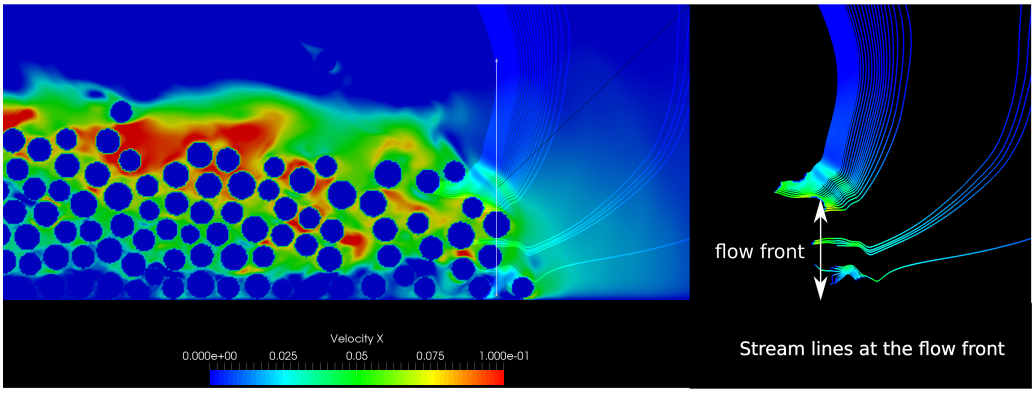

(a) streamlines at the flow front dense case (contours show velocity of fluid entrainment at the flow front)

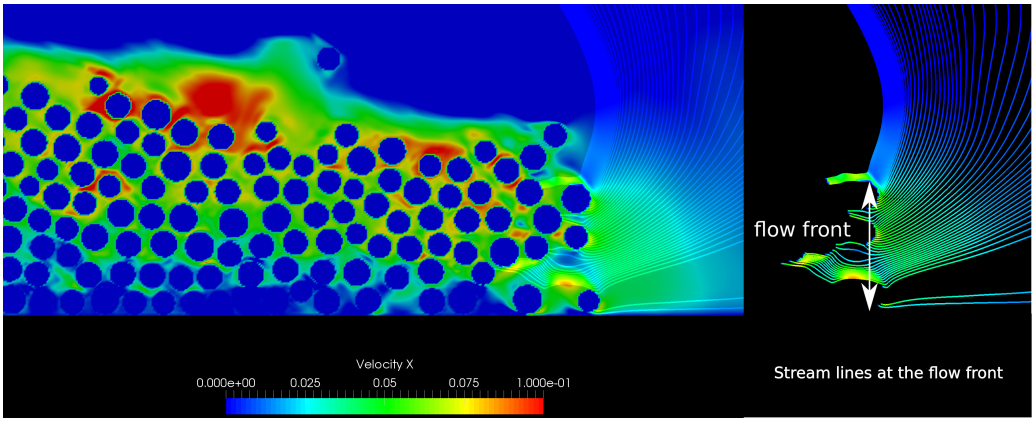

(b) streamlines at the flow front loose case (contours show velocity of fluid entrainment at the flow front)

Figure 13: Water entrainment for a slope of $5°$ (dense and loose cases).

References

[1] C. Cassar, M. Nicolas, O. Pouliquen, *Physics of Fluids* **2005**, *17*, 103301–11.

[2] B. Cook, D. Noble, J. Williams, *Engineering Computations* **2004**, *21*, 151–168.

[3] R. Denlinger, R. Iverson, *J. Geophys. Res* **2001**, *106*, 553–566.

[4] R. Du, B. Shi, X. Chen, *Physics Letters A* **2006**, *359*, 564–572.

[5] X. He, Q. Zou, L. S. Luo, M. Dembo, *Journal of Statistical Physics* **1997**, *87*, 115–136.

[6] R. M. Iverson, *Rev. Geophys.* **1997**, *35*, 245–296.

[7] K. Kumar, PhD thesis, University of Cambridge, **2015**.

[8] K. Kumar, J.-Y. Delenne, K. Soga, *Journal of Hydrodynamics Ser. B* **2017**, *29*, 529–541.

[9] S. H. Liu, D. A. Sun, Y. Wang, *Computers and Geotechnics* **2003**, *30*, 399–408.

[10] C. Meruane, A. Tamburrino, O. Roche, *Journal of Fluid Mechanics* **2010**, *648*, 381–404.

[11] M. Pailha, O. Pouliquen, M. Nicolas, *AIP Conference Proceedings* **2008**, *1027*, 935–937.

[12] S. Peker, S. Helvaci, *Solid-liquid two phase flow*, Elsevier, **2007**.

[13] A. Romano, M. Di Risio, M. G. Molfetta, G. Bellotti, D. Pasquali, P. Sammarco, L. Damiani, P. De Girolamo, *Coastal Engineering Proceedings* **2017**, *1*, 14.

[14] L. Rondon, O. Pouliquen, P. Aussillous, *Physics of Fluids* **2011**, *23*, 073301.

[15] J. Smagorinsky, *Monthly weather review* **1963**, *91*, 99–164.

[16] L. Staron, E. J. Hinch, *Granular Matter* **2007**, *9*, 205–217.

[17] S. Succi, *The lattice Boltzmann equation for fluid dynamics and beyond*, Oxford University Press, **2001**, p. 288.

[18] V. Topin, F. Dubois, Y. Monerie, F. Perales, A. Wachs, *Journal of Non-Newtonian Fluid Mechanics* **2011**, *166*, 63–72.

[19] K. Yazdchi, S. Srivastava, S. Luding, *International Journal of Multiphase Flow* **2011**.

[20] H. Yu, S. Girimaji, L. Luo, *Physical Review E* **2005**, *71*, 016708.

Authors

Dr. Krishna Kumar
Department of Engineering
University of Cambridge
Cambridge, CB2 1PZ
Tel.: +44(0) 1223 748 589
e-mail: kks32@cam.ac.uk
Web: www.cb-geo.com

Prof. Jean-Yves Delenne
IATE INRA-CIRAD-Montpellier Supagro-UM2
University of Montpellier 2
e-mail: jean-yves.delenne@supagro.inra.fr

Prof. Kenichi Soga
Department of Civil and Environmental Engineering
University of California Berkeley
California, USA
e-mail: soga@berkeley.edu
Web: www.ce.berkeley.edu/people/faculty/soga